Effects of crystal structure, size, shape and surface structural differences on photo-induced electron transport in TiO$_2$ mesoporous electrodes

Shingo Kambe,[a] Shogo Nakade,[b] Yuji Wada,[a] Takayuki Kitamura[a] and Shozo Yanagida*[a]

[a]Material and Life Science, Graduate School of Engineering, Osaka University, Suita, Osaka 565-0871, Japan. E-mail: yanagida@chem.eng.osaka-u.ac.jp
[b]Nokia Research Center, Nokia-Japan Co., Ltd., 2-13-5, Nagata-cho, Chiyoda-ku, Tokyo, Japan

Various kinds of mesoporous electrodes composed of TiO$_2$ nanocrystallites with different crystal structures (rutile or anatase), crystalline shapes, crystalline sizes and crystallinity have been prepared. The electron diffusion coefficients of these TiO$_2$ mesoporous electrodes have been determined by time-resolved photocurrent measurements. The electron diffusion coefficients of the rutile electrodes were one order of magnitude smaller than those of the anatase ones. The electrode prepared using a high crystalline anatase TiO$_2$ needed a higher annealing temperature to obtain an increased diffusion coefficient, which was explained as being due to the effective necking at higher annealing temperature. The diffusion coefficient of the rutile electrode was enhanced four times by the treatment with aq. TiCl$_4$ solution, while no significant changes were observed in the case of the anatase film electrodes. New layers of rutile TiO$_2$ with a piled-needle-like shape were produced on the surface of the rutile nanocrystallites after the treatment with aq. TiCl$_4$ solution. These newly formed rutile layers on the surface and their interface should promote the necking between the nanocrystallites at annealing, increasing the diffusion coefficient of the rutile film electrode.

Introduction

Dye-sensitized nanocrystalline TiO$_2$ solar cells have attracted great interest because of their simple structure, low cost, and efficiency of practical use. Several points should be currently considered for developing new effective sensitizing dyes,[1–8] improving the ion transport in the electrolyte systems,[9,10] optimizing morphology of TiO$_2$ electrodes,[11,12] electrode–electrolyte interface[13–20] and inter-particle connectivity in the TiO$_2$ mesoporous electrode.[12,21] Among these points, we have concentrated our attention on the photo-induced electron transport in the mesoporous electrodes and decided to reveal the effects of characteristics of TiO$_2$ nanoparticles of the mesoporous electrode on the photo-induced electron transport property.

Electron transport in the mesoporous TiO$_2$ electrodes is assumed to proceed by diffusion because of the absence of a significant electrical potential gradient in the film.[22–25] The trap states, as the electron diffusion sites, should be largely influenced by the characteristics of the TiO$_2$ nanoparticles such as crystal structure, shape and crystallinity of the nanoparticles, resulting in the changes of the transport properties. The dynamics of the electron-transport process in the mesoporous TiO$_2$ films have been studied by intensity-modulated photocurrent spectroscopy (IMPS),[22–24,26–29] time-of-flight (TOF)[29–31] and time-resolved photocurrent measurements.[25,29,32]

In this work, we have employed time-resolved photocurrent measurements in order to carry out semi-quantitative evaluation of the electron transport properties of the mesoporous TiO$_2$ electrodes. Laser flash using a photon energy exceeding the band gap of TiO$_2$ induces a transient photocurrent. The measurement of this transient photocurrent is a convenient method for the estimation of the apparent diffusion coefficient of the mesoporous TiO$_2$ films without the effects of the sensitizing dyes.

For comparison under comparable surface conditions, pure anatase and pure rutile TiO$_2$ nano-crystallites were synthesized using a common starting material and common additives. Furthermore, commercially available TiO$_2$ nanoparticles were also employed to prepare the films for wide comparison. Attention was paid to the TiCl$_4$ treatment on the mesoporous TiO$_2$ films.[4,12] It was hypothesized without any discrete evidence that the TiCl$_4$ treatment increased the necking between the nanoparticles of the film, thus facilitating the diffusion of photo-injected electrons from one particle to another and lowering the probability of recombination.[12]

In this paper, we demonstrate and discuss the relationship between the photo-induced electron transport properties and the nature of mesoporous TiO$_2$ to obtain good electron transport properties of the electrodes in dye sensitized solar cells.

Experimental

TiO$_2$ nanoparticles

Seven kinds of TiO$_2$ nanoparticles, **A1-A5**, **R1** and **R2**, were used in the present work (Table 1). **A1** and **R1** were prepared as described below. A common starting material and common additives were employed to avoid the effects of the starting material and additives on the surface properties of the TiO$_2$ nanocrystallites. During the crystallization process, we used no mineralizer that might induce undesirable effects on the surface properties.[33] Hydrothermal TiO$_2$ synthesis similar to the synthesis reported from Kumar et al. was employed without using SnO$_2$ as a seed nucleus.[34] A propan-2-ol solution (100 ml) of 0.5 M titanium isopropoxide (Wako Pure Chemical Industries) was added dropwise to a well-stirred sample of

Table 1 Characteristics of TiO_2 nanoparticles and the electron diffusion coefficients of the electrodes

	Structure[a]	Shape	Size/nm[b]	$D(\times 10^{-5})/cm^2 s^{-1}$
A1	A/Amor	Spherical	12	2.2
A1$_{TiCl_4}$[c]	A/Amor	Spherical	12	2.2
A2	A	Cubic	12	0.3
A2$_{550}$[d]	A	Cubic	12	2.0
A3 (CCI)	A	Rod-like	13/34	4.0
A4 (CCI)	A	Cubic	11	4.1
A5 (P25)	A/R	Spherical	21	4.0
A5$_{Large}$[e]	A/R	Spherical	21	4.0
R1	R	Spherical	27	0.1
R1$_{TiCl_4}$[c]	R	Spherical	27	0.4
R2 (CCI)	R	Rod-like	23/73	0.3

[a] A = anatase structure, Amor = amorphous phase, R = rutile structure. [b] Average size. [c] Treated with aq. $TiCl_4$ solution. [d] Annealed at 550 °C. [e] With 20 wt% of large TiO_2 (Fluka).

propan-2-ol (364 ml) containing H_2O (36 ml). The solution was stirred for 1 h and the resulting precipitate was washed with water and then filtrated. The obtained white gel was redispersed in H_2O with nitric acid. Solutions were refluxed at 80 °C for 12 h and then autoclaved at 220 °C for 12 h. Anatase and rutile TiO_2 colloids were selectively prepared by controlling the pH during autoclaving. The rutile crystal structure (denoted **R1**) and the anatase crystal structure (denoted **A1**) were obtained at pH 0.5 and pH 1.3, respectively. **A1** had spherical shape with an average particle size of 12 nm, containing a small amount of brookite crystal structure, which disappeared by annealing at 450 °C. **R1** had spherical shape with an average size of 27 nm. **A2** was synthesized by hydrothermal synthesis of amorphous TiO_2 prepared through hydrolysis of $TiCl_4$ with Na_2CO_3 in the presence of HF and HCl as catalysts for obtaining higher crystallinity, *i.e.* absence of the amorphous phase.[35] **A2** nanoparticles had an anatase crystal structure with cubic shape and an average size of 12 nm.

A3 was supplied by Catalysis & Chemicals Ind. Co., Ltd. (denoted as CCI, hereafter), having an anatase crystal structure, a rod-like shape and an average size of 13 × 34 nm (HPW-25R). **A4** was also supplied by CCI, having the anatase crystal structure, cubic shape and an average size of 11 nm (HPW-10R). **A5** was supplied by Nippon Aerosil, having a mixed crystal structure (anatase : rutile = 8 : 2), a spherical shape and an average size of 21 nm (P25). **R2** was supplied by CCI, having a rutile crystal structure, rod-like shape and an average size of 23 × 73 nm (HPR-16).

Mesoporous film electrode preparations

Autoclaved **A1** sol was mixed with Fluka TiO_2 particles (size *ca.* 100 nm, 0.8 g) in a 100 ml plastic bottle and then mechanically dispersed using a paint shaker (Red Devil 5400) in the presence of zirconia beads (3 mm, 70 g). The resulting **A2** sol was condensed by evaporation so that the sol (10 wt%) was obtained and used as the paste for making the film. **A3** powder (6.0 g) was mixed with Fluka TiO_2 particles (1.2 g), acetyl acetone (Wako Pure Chemical Industries, 0.2 ml) and distilled water (12 ml), and then mechanically dispersed, giving the **A3** paste. The dispersed **A4** paste was also prepared by the same method as the **A3** paste. **A5** (P25) powder (6.0 g) was mixed with acetyl acetone (0.2 ml) and distilled water (7.0 ml) in a 100 ml plastic bottle and then mechanically dispersed, giving the **A5** paste. **R1** was dispersed by mechanical shaking after autoclaving, being then used as a paste. The dispersed **R2** paste was prepared by the same method as for the **A5** paste.

The two parallel edges of the transparent conducting glass (ASAHI GLASS Ind. Co., Ltd., F-doped SnO_2) were covered with adhesive tape (3M Scotch Mending Tape, 100 μm thick) to control the thickness of the TiO_2 films and to provide

non-coated areas for electrical contact. The dispersed paste was applied to one of the edges of the conducting glass and distributed by sliding a glass rod over the tape-covered edges (the doctor blade method). All electrodes were annealed at 450 °C for 30 min in air after drying. The film thickness could be increased by repetition of applying the sol paste and annealing.

TiCl₄ treatment

The method of the $TiCl_4$ treatment was identical with that of the previous report.[4,12] An aqueous solution of $TiCl_4$ (0.2 M) was prepared using $TiCl_4$ (Wako Pure Chemical Industries) and deionized water, and the solution was dropped on to the annealed films. The film was kept for 12 h in a closed chamber and then rinsed with distilled water. The film was annealed again at 450 °C for 30 min (the resintering process).

Characterization

Film thickness was measured using a profiler (Sloan Dektak3). X-Ray diffraction patterns were used to determine the crystal structure, the relative amount of each crystal structure, and the crystallite size using a Rigaku X-ray diffractometer with Cu-Kα radiation (λ = 1.5406 Å). The average crystallite size of the TiO_2 was calculated from the Scherrer formula. Particle size and shape were measured by TEM (JEOL JEM-2010 transmission electron microscope). A small amount of TiO_2 powder was dispersed in ethanol and the resulting suspension was deposited on to a carbon coated copper grid. SEM (JEOL JSM6700F) and Raman spectroscopy (PERKIN ELMER Spectrum GX NIR FT-Raman, 1064 nm line of an Nd-YAG laser as the excitation source, resolution 1.0 cm^{-1}, integration number of 128) were used for the characterization of the TiO_2 surface structure. The BET surface area and the pore size distribution were determined by a nitrogen adsorption apparatus (QUANTACHROME AUTOSORB-1).

Time transient photocurrent measurement

A set-up of the time transient photocurrent measurement is shown in Fig. 1. The measurements were performed in a cell made of quartz with a hole of 8 mm diameter at one side and a window at the opposite side for light irradiation. The TiO_2 mesoporous electrode of area 12 × 12 mm was fixed at the hole with a rubber O-ring. A platinum wire was used as a counter electrode. An electrolyte solution was composed of $LiClO_4$, 0.7 M and spectroscopic grade ethanol (Wako Pure Chemical Industries). The potentiostat used was a TOHO TECHNICAL
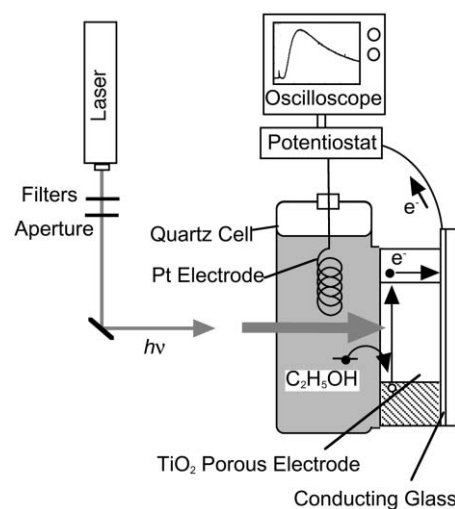
Fig. 1 Scheme of the set-up for the time transient photocurrent measurement.

RESEARCH Potentiostat/Galvanostat 2000. The transient current was monitored by a digital oscilloscope (Tektronix TDS 3052, 500 MHz). The light source was a 10 Hz Nd-YAG laser (The Quanta-Ray INDI Series, intensity 0.98 mJ cm^{-2}, pulse width 7 ns, wavelength 355 nm). Filters were employed to prevent the effects of the 2-fold and 4-fold wavelength light. The light intensity was controlled by filters. The geometric area of a electrode was fixed as 0.093 cm^{-2} by an aperture. All the measurements were performed in air with at least 3 min intervals between measurements.

Analysis

When the electrode is illuminated from the TiO$_2$-electrolyte interface side, the excited electrons are generated at the electrode surface, since the absorption coefficient of TiO$_2$ in the UV region is large (*ca.* 10^{-7} m^{-1}). The charge separation in the TiO$_2$ electrode after laser excitation is in the subnanosecond range. The hole at the valence band of TiO$_2$ is rapidly removed by supplying an electron from ethanol, thus suppressing initial electron–hole pair recombination inside the crystallites. The photogenerated electrons should be formed effectively not only from alcohol but also from the alcohol cation radical produced by the perfect current doubling effect due to the presence of perchlorate anion in the system.[36] Electrons, which are generated at the shallow region of the TiO$_2$ electrode by the pulse irradiation from the electrolyte side, move because of thermal fluctuations in the system causing a random walk process, *i.e.* a diffusion process. The electron diffusion coefficient of the mesoporous TiO$_2$ electrode can be estimated by analyzing the photocurrent transient response using the Fick's second law. With neglecting a current due to electrostatic repulsion in the solution of the time-dependent diffusion equation, the time for the current maximum, t_{peak}, appears when

$$t_{peak} = W^2/6D \qquad (1)$$

where D is the electron diffusion coefficient, and W is film thickness.[25] According to eqn. (1) we expect a linear dependence between the square of the film thickness and the time for the photocurrent maximum with a slope of D.

Results and discussion

Photocurrent time transients and their analysis using the diffusion model

Transient curves of the typical photocurrent observed for the films having different thicknesses are shown in Fig. 2. Current peaks in the photocurrent were observed by the irradiation of the laser pulse of all the samples. Minor current peaks were also observed just after the irradiation for all the samples, showing similar amplitudes. Solbrand *et al.* reported the similar behavior in the transient curves and attributed the first minor peak to reorganization of charges after the laser pulse excitation.[25] We then focused our attention only on the main rise in the current observed in the millisecond (ms) order.

The positions of the peaks in the current rise were shifted to longer times with increasing the film thickness, indicating that the electrons should travel the longer distance to reach the conducting glass layer. The decay of the current was slower for the samples with larger thickness. Therefore, the experimental observations were qualitatively in agreement with those expected for the diffusive process of electrons in the films. The maximum amplitude of the peak also decreased with increasing the film thickness. The generated charge was evaluated as 1.2 µC for the electrode with 5 µm in thickness by integrating the transient curve between the time 0 and 100 ms, and decreased to 0.5 µC for that with 15 µm in thickness, probably due to the back electron transfer to
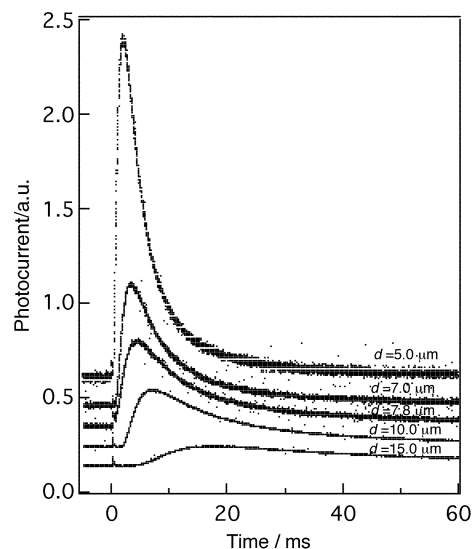

Fig. 2 Transient photocurrent spectra obtained for the **A1** electrodes with different thicknesses (denoted as the '*d*' values).

electron acceptors in the electrolyte solution such as dissolved oxygen or oxidized ethanol. However, a slight decrease in the amount of photogenerated electrons within a 12 µm thick sample was confirmed under the same light intensity. The penetration depth of the light pulse should be shallow and around hundreds of nanometers because of the high absorption coefficient of TiO$_2$ in the UV region.[25]

Fig. 3 shows W^2 *vs.* the peak time, t_{peak}, for the electrodes made with the TiO$_2$ samples. A straight line was obtained not only for **A1** but also for the other samples, indicating that the transport of electrons in these TiO$_2$ electrodes would follow the diffusion model described in the experimental section so that we determined the diffusion coefficients of electrons (denoted as D, hereafter) for comparing the electron transport properties of the TiO$_2$ films made with different TiO$_2$ nanoparticles.

The film preparation using **A1**, **A3** and **A4** sols without cracks was found to require the addition of a small amount of the large TiO$_2$ particles. Then in order to examine the effect of the added large particles on D, the **A5** electrode containing 20 wt% of the Fluka 100 nm TiO$_2$ particles was prepared and its D value determined. D_{A5} was not changed by the addition of 20 wt% of the Fluka 100 nm particles ($D_{A5_{Large}}$) when compared to the D value in their absence, ensuring that we were able to compare the electron transport properties using the D values of all the electrodes made from the TiO$_2$ nanoparticles irrespective of the presence (*ca.* 20%) of larger nanoparticles.
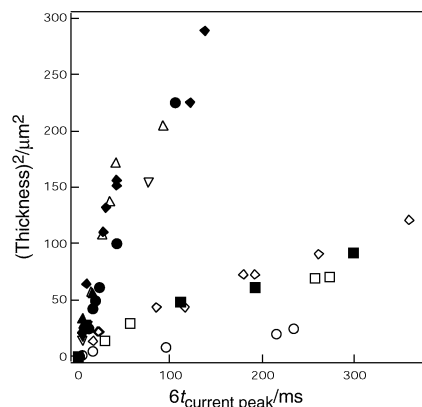

Fig. 3 The current peak *vs.* the square of each different film thickness for **A1** (●), **A2** (■), **A3** (▲), **A4** (▼), **A5** (◆), **R1** (○), **R2** (□), **A5** with 20 wt% Fluka particles (△), 550 °C sintered **A2** (▽), and **R1** with TiCl$_4$ treatment (◇).

The D values determined for all the electrodes made from the TiO_2 samples are listed in Table 1. In a general comparison, the electron diffusion coefficients of the rutile electrodes (D_{R1} and D_{R2}) were almost one order of magnitude smaller than those of the anatase electrodes (D_{A1}, D_{A3}, D_{A4} and D_{A5}). Similar diffusion coefficients were obtained for **A3** and **A4**, which were prepared by the common synthesis method, but possessed different particle sizes and shapes.[37] The **A2** electrode having the anatase structure with higher crystallinity than **A1** gave a smaller D value. However, the D value was much increased by annealing at 550 °C, being close to that of D_{A1}. The detailed comparison of the diffusion was discussed from the viewpoints of crystal structure, size and shape, and effect of the $TiCl_4$ treatment.

Effects of crystal structure

The D values of the **R1** and **R2** electrodes were 0.1×10^{-5} and 0.3×10^{-5} cm^2 s^{-1}, respectively, whereas those of the anatase electrodes except that of **A2** annealed at 450 °C were in the range of $(2.0–4.1) \times 10^{-5}$ cm^2 s^{-1}. The D values of the rutile electrodes were almost one order of magnitude lower than those of the anatase electrodes, although it was not strongly dependent upon the crystal size and shape. This indicates that electron transport in mesoporous TiO_2 is predominantly influenced by crystal structure rather than crystal size and shape. A remarkable difference between the D values of anatase and rutile electrodes is observed by a comparison of D_{A1} (2.2×10^{-5} cm^2 s^{-1}) with D_{R1} (0.1×10^{-5} cm^2 s^{-1}). Because **A1** and **R1** particles were prepared under the similar conditions, the difference was attributed to the intrinsic effect of the crystal structures.

The electron transport properties of the rutile and the anatase have been reported previously.[38,39] The smaller D values of the mesoporous rutile electrodes were also confirmed by the IMPS measurements for the dye-sensitized electrode.[40] The rutile nanoparticles are more resistant to sintering at annealing than the anatase ones. This fact may be one of the possible reasons for the lower D values. The importance of the neck growth due to sintering is also shown by the result that neck growth in **R1** electrodes caused by aq. $TiCl_4$ treatment increases the D values (discussed below).

Effects of crystallinity, crystal size and shape

D_{A2} (0.3×10^{-5} cm^2 s^{-1}) was one order of magnitude smaller than D_{A1} (2.2×10^{-5} cm^2 s^{-1}), whereas **A1** and **A2** particles have a similar crystalline size and shape. D_{A2} was increased to 2.0×10^{-5} cm^2 s^{-1} by annealing at a higher temperature (550 °C), which was comparable to D_{A1}. Fig. 4 shows the XRD patterns of **A1** and **A2** particles. All the peaks in the pattern of **A2** are assigned to anatase crystal structure and these sharp pe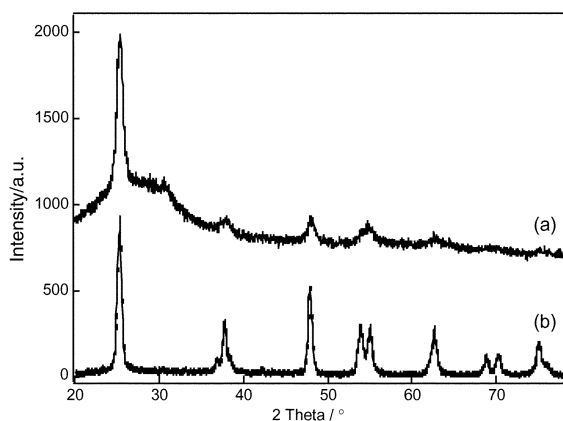aks indicate that **A2** consists of well-crystallized pure anatase. On the other hand, the broad band at around 25–30° in the pattern of **A1** indicates that **A1** contained some amorphous phase. The peak at 32° was assigned to a small amount of the brookite crystal structure. The amorphous and brookite crystal structures contained in **A1** disappeared by annealing at 450 °C. Considering that the TiO_2 film made from **A1**, i.e. TiO_2 particles with lower crystallinity, gave a higher diffusion coefficient, the presence of the amorphous phase in the starting TiO_2 nanoparticle should be effective for increasing the electron transport probably because the amorphous phase should enhance the necking between particles by sintering at 450 °C. On the other hand, **A2** electrodes require heating at higher temperature for sintering because of the absence of the amorphous phase. It is considered that the particle-necking rather than the crystallinity of the particles predominantly affects the electron transport. No morphological differences in SEM images between the **A2** electrodes annealed at 450 and 550 °C were observed, indicating that the particle-necking occurs in the scale of atomic order. **A3** and **A4** particles synthesized under comparable conditions (according to CCI) had different crystal sizes and shapes (Table 1). There was no significant difference between D_{A3} (4.0×10^{-5} cm^2 s^{-1}) and D_{A4} (4.1×10^{-5} cm^2 s^{-1}) in this study. However, the effect of the size and shape on D needs more detailed study and the work is in progress.

Effect of the treatment with aq. $TiCl_4$ solution

D_{R1} was increased four-fold by the $TiCl_4$ treatment, though no significant changes were observed in the case of the **A1** electrode. We performed the detailed analyses of the morphological changes of the mesoporous rutile TiO_2 electrodes in order to elucidate the relationship between the electron transport properties and the surface changes of the mesoporous TiO_2 electrodes caused by the $TiCl_4$ treatment. Changes in the SEM images of the **R1** electrode during the $TiCl_4$ treatment are shown in Fig. 5. Fig. 5(a) shows that the **R1** electrode consists of nanoparticles with a size of ca. 27 nm before the treatment (denoted as sample **a**). Just after dropping the $TiCl_4$ aqueous solution on to the electrode and washing it, new layers with piled-needle-like shapes were produced on the rutile nanoparticle surface [sample **b**, Fig. 5(b)]. These new layers disappeared by re-annealing and the particle-necking was confirmed for sample **c**, as in Fig. 5(c).

BET surface areas and pore size distributions were also compared before and after the $TiCl_4$ treatment. The BET surface area of the sample **b** was increased to 70.3 m^2 g^{-1} from 44.9 m^2 g^{-1} when compared with that of the sample **a**, and the pore volume, having a pore diameter of less than 5 nm, was also increased when the sample **b** was compared with sample **a**. These changes of BET surface area and pore volume should be the reflection of the morphological change as observed in the SEM. Sample **c** gave a decrease in the surface area (35.5 m^2 g^{-1}) and in the pore volume in the small size region. Formation of the piled-needle-like structure and its disappearance by sintering can explain the results of the measurements of the BET surface area and pore size distributions.

Fig. 6 shows the changes to the Raman spectra of the 7.9 μm thick **R1** electrode during the $TiCl_4$ treatment. Before treatment (sample **a**), the peaks at 240, 450, 610 cm^{-1} assigned to the vibrational modes of the TiO_2 rutile structure were obtained [Fig. 6(a)]. The intensities of the peaks were enhanced and the peaks were sharpened for sample **b** compared with those in sample **a** [Fig. 6(b)], exhibiting the generation of new rutile layers on the rutile TiO_2 surface. This result demonstrates epitaxial growth of rutile layers on the electrode surface, which is made entirely of rutile nanoparticles by dropping the aqueous $TiCl_4$ solution when taking into account the SEM image [Fig. 5(b)]. During the resintering process no clear change in the Raman spectrum was observed [Fig. 6(b) and (c)].
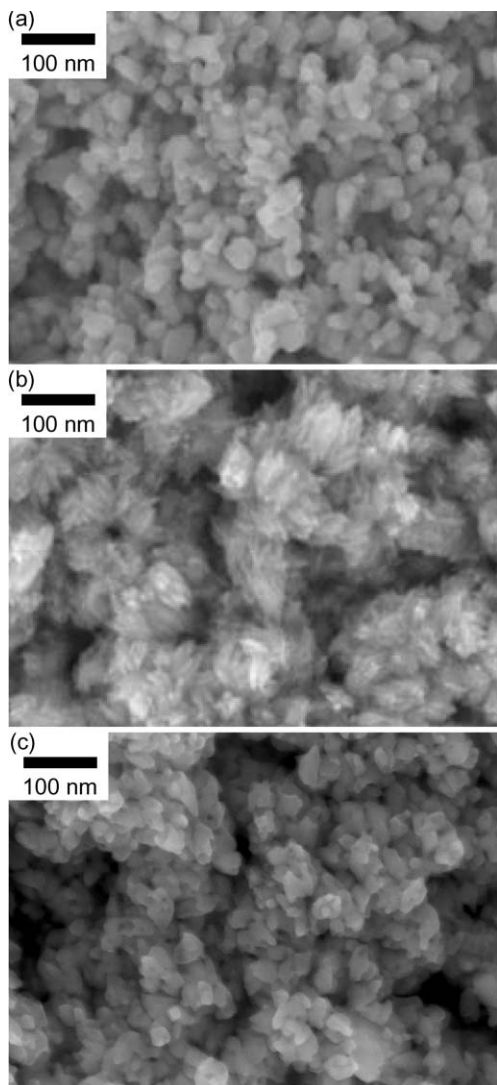

Fig. 4 XRD patterns of **A1** particles (a) and **A2** particles (b).

Fig. 5 SEM images of **R1** films before the TiCl₄ treatment (a), after the TiCl₄ treatment without resintering (b), and after the TiCl₄ treatment with resintering (c).
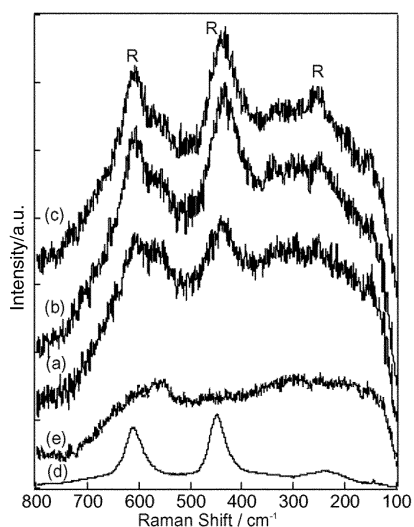

Fig. 6 Raman spectra of the **R1** films on the conducting glass before the TiCl₄ treatment (a), after the TiCl₄ treatment without resintering (b), and after the TiCl₄ treatment with resintering (c). Typical spectra for rutile (d) and the glass substrate (F-SnO₂) (e) are also shown as references.

These results show that the new rutile layers with piled-needle-like shapes were fused with the original particles and induce the particle-necking

Hildenbrand and his colleagues have obtained the high similarity in the X-ray absorption near edge structure (XANES) between $TiCl_4$ aqueous solutions and anatase TiO_2.[41] Considering this fact, selective formation of the rutile layers in the $TiCl_4$ treatment should be explained by the surface epitaxial growth that strongly depends on the surface structure. The newly generated rutile layers should connect the nanoparticles during re-annealing at 450 °C and increase the electron transport properties of the **R1** electrode. The $TiCl_4$ treatment would be useful as the surface modification method, which induces effective particle-necking in rutile mesoporous TiO_2 electrodes.

Conclusions

Mesoporous TiO_2 films have been prepared by using seven varieties of TiO_2 nanoparticles with different crystal structures, sizes and shapes. The electron diffusion coefficients of the mesoporous TiO_2-electrolyte system have been estimated by time-resolved photocurrent measurements. The electron diffusion coefficients of the rutile electrodes were smaller than those of the anatase electrodes. The amorphous phase around the nanoparticles was found to be effective for necking between particles at relatively low temperatures. The electron diffusion in the electrodes composed of anatase nanoparticles with high crystallinity was enhanced only by annealing at higher temperature. The electron transport properties of the mesoporous rutile TiO_2 electrode were enhanced by the $TiCl_4$ treatment, because the new rutile layer was generated by the treatment, enhancing the connection between rutile particles.

References

1 M. K. Nazeeruddin, P. Pechy, T. Renouard, S. M. Zakeeruddin, R. Humphry-Baker, P. Comte, P. Liska, L. Cevey, E. Costa, V. Shklover, L. Spiccia, G. B. Deacon, C. A. Bignozzi and M. Grätzel, *J. Am. Chem. Soc.*, 2001, **123**, 1613.
2 S. M. Zakeeruddin, M. K. Nazeeruddin, P. Pechy, F. P. Rotzinger, R. Humphry-Baker, K. Kalyanasundram and M. Grätzel, *Inorg. Chem.*, 1997, **36**, 5937.
3 M. K. Nazeeruddin, R. Humphry-Baker, M. Grätzel and B. A. Murrer, *J. Chem. Soc., Chem. Commun.*, 1988, 719.
4 M. K. Nazeeruddin, A. Kay, I. Rodicio, B. R. Humphry, E. Mueller, P. Liska, N. Vlachopoulos and M. Grätzel, *J. Am. Chem. Soc.*, 1993, **115**, 6382.
5 M. K. Nazeeruddin, P. Pechy and M. Grätzel, *J. Chem. Soc., Chem. Commun.*, 1998, 1705.
6 M. K. Nazeeruddin, S. M. Zakeeruddin, R. Humphry-Baker, M. Jirousek, P. Liska, N. Vlachopoulos, V. Shklover, C.-H. Fischer and M. Grätzel, *Inorg. Chem.*, 1999, **38**, 6298.
7 V. Shklover, M. K. Nazeeruddin, S. M. Zakeeruddin, C. Barbé, A. Kay, T. Haibach, W. Steurer, R. Hermann, H.-U. Nissen and M. Grätzel, *Chem. Mater.*, 1997, **9**, 430.
8 H. Sugiura, L. P. Singh, K. Sayama, A. Hironori, M. K. Nazeeruddin and M. Grätzel, *Chem. Lett.*, 1998, 1005.
9 N. Papageorgiou, C. Barbe and M. Grätzel, *J. Phys. Chem. B*, 1998, **102**, 4156.
10 Z. Kebede and S. Lindquist, *Sol. Energy Mater. Sol. Cells*, 1998, **51**, 291.
11 L. Kavan, M. Grätzel, J. Rathousky and A. Zukal, *J. Electrochem. Soc.*, 1996, **143**, 394.
12 C. J. Barbe, F. Arendse, P. Comte, M. Jirousek, F. Lenzmann, V. Shklover and M. Grätzel, *J. Am. Ceram. Soc.*, 1997, **80**, 3157.
13 N. J. Cherepy, G. P. Smestad, M. Grätzel and J. Z. Zhang, *J. Phys. Chem. B*, 1997, **101**, 9342.
14 R. J. Ellington, J. B. Asbury, S. Ferrere, H. N. Ghosh, J. R. Sprague, T. Lian and A. J. Nozik, *J. Phys. Chem. B*, 1998, **102**, 6455.
15 S. A. Haque, Y. Tachibana, R. L. Willig, J. E. Moser, M. Grätzel, D. R. Klung and J. R. Durrant, *J. Phys. Chem. B*, 2000, **104**, 538.
16 Y. Tachibana, J. E. Moser, M. Grätzel, D. R. Klug and J. R. Durrant, *J. Phys. Chem.*, 1996, **100**, 20 056.

17 Y. Tachibana, S. A. Haque, I. P. Mercer, J. R. Durrant and D. R. Klug, *J. Phys. Chem. B*, 2000, **104**, 1198.
18 J. B. Asbury, R. J. Ellingson, H. N. Ghosh, S. Ferrere, A. J. Nozik and T. Lian, *J. Phys. Chem. B*, 1998, **102**, 6455.
19 B. Burfeindt, T. Hannappel, W. Storck and F. Willig, *J. Phys. Chem.*, 1996, **100**, 16 463.
20 G. A. Gregg, F. Pichot, S. Ferrere and C. L. Fields, *J. Phys. Chem. B*, 2001, **105**, 1422.
21 S. Kambe, K. Murakoshi, T. Kitamura, Y. Wada, S. Yanagida, H. Komonami and Y. Kera, *Sol. Energy Mater. Sol. Cells*, 2000, **61**, 427.
22 P. E. de Jongh and D. Vanmaekelbergh, *J. Chem. Phys. B*, 1997, **101**, 2716.
23 F. Cao, G. Oskam, G. J. Meyer and P. C. Searson, *J. Phys. Chem.*, 1996, **100**, 17 021.
24 L. Dloczik, O. Ileperuma, I. Lauermann, L. M. Peter, E. A. Ponomarev, G. Redmond, N. J. Shaw and I. Uhlendrf, *J. Phys. Chem. B*, 1997, **101**, 10 281.
25 A. Solbrand, H. Lindstrom, H. Rensmo, A. Hagfeldt, S. Lindquist and S. Sodergren, *J. Phys. Chem. B*, 1997, **101**, 2514.
26 L. M. Peter and D. Vanmaekelbergh, *Adv. Electrochem. Sci. Eng.*, 1999, **6**, 77.
27 J. van de Lagemaat and A. J. Frank, *J. Phys. Chem. B*, 2000, **104**, 4292.
28 B. van der Zanden and A. Goossens, *J. Phys. Chem. B*, 2000, **104**, 7171.
29 N. Kopidakis, E. A. Schiff, N.-G. Park, J. van de Lagemaat and A. J. Frank, *J. Phys. Chem. B*, 2000, **104**, 3930.
30 T. Dittrich, E. A. Lebedev and J. Weidmann, *Phys. Status Solidi A*, 1998, **165**, R5.
31 T. Dittrich, *Phys. Status Solidi A*, 2000, **182**, 447.
32 S. Nakade, S. Kambe, T. Kitamura, Y. Wada and S. Yanagida, *J. Phys. Chem. B*, 2001, **105**, 9150.
33 S. T. Aruna, S. Tirosh and A. Zaban, *J. Mater. Chem.*, 2000, **10**, 2388.
34 K.-N. P. Kumar, K. Keizer, A. J. Burggraaf, T. Okubo and H. Nagamoto, *J. Mater. Chem.*, 1993, **3**, 923.
35 H. Yin, T. Kitamura, S. Kambe, S. Murasawa, H. Mori, T. Sakata and S. Yanagida, *J. Mater. Chem.*, 2001, **11**, 1694.
36 S. R. Morrison, *Electrochemistry at Semiconductor and Oxidized Metal Electrodes*, Plenum Press, New York, 1980, p. 213.
37 Detailed preparation conditions of **A3** and **A4** cannot be given because they are the company's products. At least the starting materials are the same and the preparation methods are essentially similar.
38 A. Wahl and J. Augustynski, *J. Phys. Chem. B*, 1998, **102**, 7820.
39 H. Tang, H. Berger, P. E. Schmid, F. Levy and G. Burri, *Solid State Commun.*, 1993, **87**, 847.
40 N.-G. Park, J. van de Lagemaat and A. J. Frank, *J. Phys. Chem. B*, 2000, **104**, 8989.
41 V. D. Hildenbrand, H. Fuess, G. Pfaff and P. Reynders, *Z. Phys. Chem.*, 1996, **194**, 139.